

High-power-density sputtering of industrial-scale targets: Case study of (Al,Cr)N

F.F. Klimashin^{a,*}, J. Kluson^b, M. Učík^{b,c}, R. Žemlička^{d,1}, M. Jílek^b, A. Lümkmann^d,
J. Michler^a, T.E.J. Edwards^a

^a Empa – Swiss Federal Laboratories for Materials Science and Technology, Feuerwerkerstrasse 39, 3602 Thun, Switzerland

^b PLATT a.s., Průmyslová 3020, 787 01 Šumperk, Czech Republic

^c Masaryk University, Kotlářská 2, 611 37 Brno, Czech Republic

^d PLATT AG, Eichholzstrasse 9, 2545 Selzach, Switzerland

ARTICLE INFO

Keywords:

Movable magnetron
High-power-density sputtering
AlCrN
Microstructure
Fracture toughness
Cutting performance

ABSTRACT

Large-scale sputter-deposition of hard protective coatings has not been prevalent as the large dimensions of the industrial targets posed an enormous technological challenge: only relatively low power (and plasma) densities could be achieved, resulting ultimately in poor performance of such coatings. Here, we introduce a novel sputtering technology allowing to reach high power densities for industrial tubular targets. This is realised on the principle of a longitudinal movement of a reduced-size magnetron inside the target. In doing so, peak power densities of 840 W/cm² have been achieved for the overall power of 25 kW and the target dimensions of Ø110 × 510 mm. To demonstrate the effectiveness of the solution, we produced a series of cubic (Al,Cr)N coatings by sputtering an Al₆₀Cr₄₀ target. Most of the coatings have a stoichiometric composition, smooth surface and a moderate amount of growth defects. Significant improvements through recipe optimisation could be achieved resulting in mechanical properties (hardness, fracture toughness, wear resistance) being equal to and even exceeding those of the benchmark coatings produced by means of conventional sputtering and cathodic arc evaporation. Our results open up great potential of this novel sputtering technique for the coating industry.

1. Introduction

Hard protective coatings for industrial applications are usually produced by means of cathodic arc evaporation (CAE). The process is characterised by a high ionisation degree of the evaporated material and fast growth of highly dense coatings. On the downside, the inherent microscopic growth defects like droplets reduce density and increase roughness of the coatings and can act as stress concentrators leading to the formation of cracks. This has a negative effect on the properties and wear resistance of the coatings [1]. Although these limitations could be overcome by utilising a sputtering process, the large dimensions of the industrial targets pose an enormous technological challenge as rather small power and plasma densities can be achieved resulting ultimately in underperformance of sputter-deposited coatings.

Here, we introduce a novel coating deposition technology allowing one to achieve high plasma power densities even for the large-scale targets – the moving focussed magnetic field magnetron sputtering

(hereafter *F-MS*). This is realised by longitudinal movement of a reduced size magnetron inside a tubular target (see Fig. 1a-c). By using a DC power supply with a total output power of 25 kW and a target measuring Ø110x510 mm, we attained peak sputter power densities of 840 W/cm² – a six-fold increase compared to a conventional magnetron (hereafter DCMS, see Fig. 1d), with an even more pronounced impact on larger targets. Power densities reached in the *F-MS* and DCMS processes are characteristic of high power impulse (HiPIMS) and modulated pulse power (MPP) magnetron sputtering [2,3] yet with considerably higher duty cycles (Fig. 1e). This is enabled through highly effective cooling in tubular targets [4,5], which is furthermore improved by moving magnetron (*F-MS*) and target rotation (DCMS). High duty cycles allow one to achieve high deposition rates (Fig. 1f) and ultimately greater productivity.

To demonstrate the effectiveness of the novel technology, we deposited coatings made of a solid solution of aluminium and chromium nitrides with a face-centred cubic structure fcc-(Al,Cr)N – a material

* Corresponding author.

E-mail address: fedor.klimashin@empa.ch (F.F. Klimashin).

¹ Current affiliation: Evatec AG.

system which has been a subject of numerous research activities since 1990 [6–9] and became of a tremendous industrial importance in 2003, when the need for higher cutting speeds (and thus operating temperatures) created buoyant demand for higher oxidation resistance [10]. (Detailed description of the material system and a great deal of useful insights can be found, for instance, in the recent comprehensive review article by J. Vetter et al. [11] and references therein.) The coatings were deposited here from an $\text{Al}_{60}\text{Cr}_{40}$ target using different nitrogen pressure, p_{N_2} , and bias voltage, $-U_s$. We also varied the magnetic flux density (hereafter B) by sputtering pristine and substantially thinned targets (Fig. 1d). The mechanical and cutting test results of our F -MS hard coatings found their hardness and wear rates already equal to those of current state-of-the-art CAE coatings, which opens up great potential of this sputtering technique for the coating industry.

2. Results

To provide insights into the process-microstructure-properties relationship of the novel F -MS coatings, a systematic chemical and structural characterisation of microstructures of the deposited coatings was carried out. All F -MS coatings have a smooth surface and a moderate volume fraction of growth defects (See SEM micrographs of the surface of a few selected coatings in Supplementary Material, Fig. S1). X-ray diffraction experiments in a Bragg-Brentano configuration (BBXRD) revealed that all coatings were, as anticipated, single-phase face-centred cubic (see Fig. 2 and Fig. S2 in Supplementary Material). Besides, all coatings show a (111) preferential growth texture. Increasing p_{N_2} and bias voltage result in a shift of the reflections to lower 2θ angles, which might be caused by expanding crystal lattice or increasing compressive in-plane residual stresses. Higher nitrogen pressures result also in attenuation of the intensity. It is noteworthy that only the coating deposited at 0.12 Pa and 60 V has a distinctly different peak shape suggesting significantly smaller grain size and possibly the presence of Al- and Cr-rich (Al,Cr)N segregated grains. The atomic fractions $\text{Al}/(\text{Al} + \text{Cr})$ and $\text{N}/(\text{Al} + \text{Cr})$ change only slightly, within the measurement accuracy.

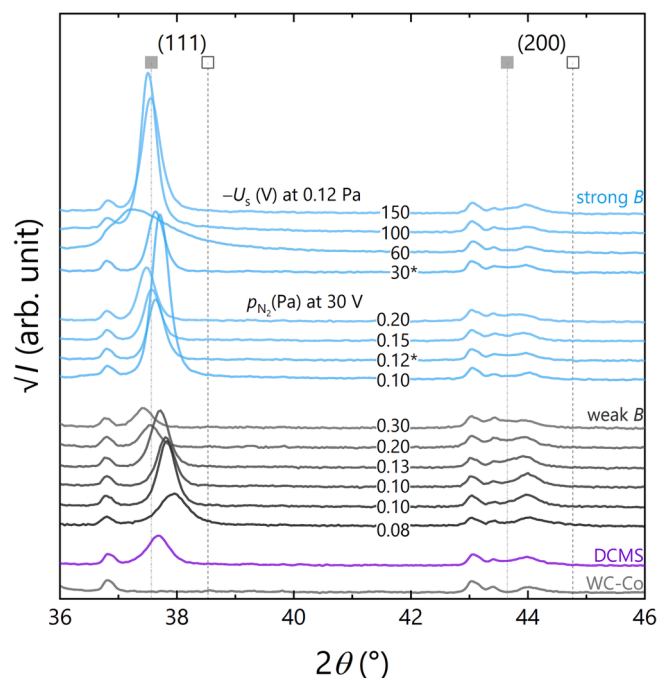


Fig. 2. X-ray diffraction patterns (Bragg-Brentano configuration) of the F -MS coatings showing the (111) and (200) reflections. (The full-angular-range diffractograms are given in Supplementary Material, Fig. S2a.) The vertical reference lines indicate fcc-CrN (ICSD 192945) and fcc-AlN (ICSD 608628). The two coatings deposited at $p_{\text{N}_2} = 0.10$ Pa (weak B) differ in thickness (4.2 μm below and 2.7 μm above).

The results of the microstructural investigations based on glancing angle XRD (GAXRD) experiments indicate that higher nitrogen pressures result in larger stress-free lattice parameter, a_0 (see Fig. 3 and Fig. S3 for GAXRD patterns). The a_0 values increase from 4.0970 to 4.1448 Å as the

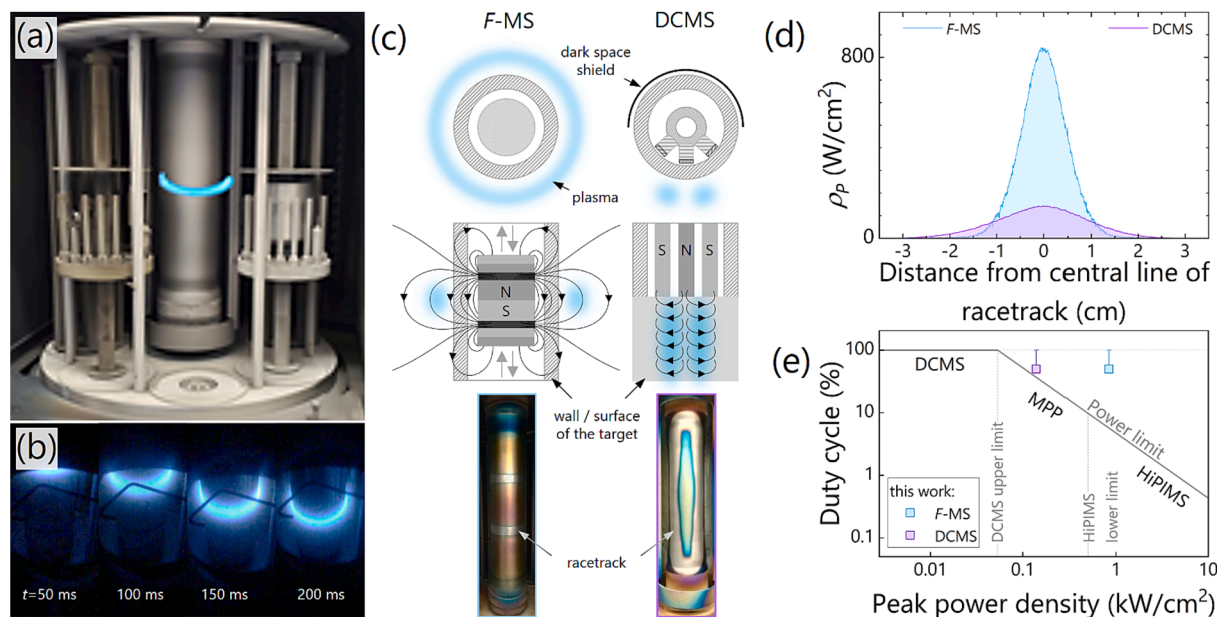


Fig. 1. Overview of Platin $\pi 411$ chamber with schematised annular blue plasma generated by the movable focussed magnetic field (a), directly imaged plasma moving along the height of a tubular metal target during operation in the 4 panes (b). Schematics of the magnetron assembly for the F -MS and DCMS modes (top and side view) and the photographs of the target after a short run (note that for the F -MS mode, the racetracks were produced without moving the magnetron) (c). The power densities achieved in the F -MS and DCMS modes at 25 kW (d) for the racetrack areas labelled in (c). Power density–duty cycle plot modified after Gudmundsson et al. [3] (e). Duty cycle of 100% is possible in the DCMS process due to rotation of the tubular targets. For the F -MS process, duty cycle provides a lower bound by taking into account the operation time when the deposition rate remains above 50% of its peak value. A video of the sputtering process is shown in Supplementary Material Video 1. (For interpretation of the references to colour in this figure legend, the reader is referred to the web version of this article.)

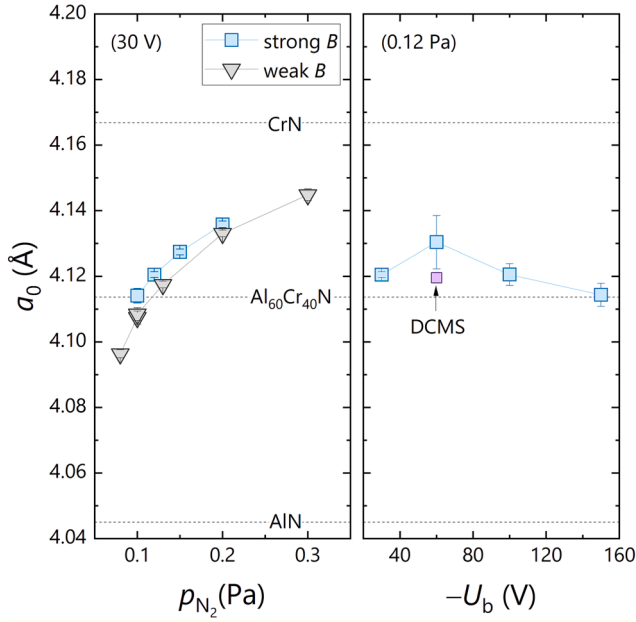


Fig. 3. Stress-free lattice parameter of the *F*-MS coatings deposited from $\text{Al}_{60}\text{Cr}_{40}$ target at different nitrogen pressures and bias voltages. The dotted lines represent the lattice parameter of fcc-CrN (4.1668 Å, ICSD 192945), fcc-AlN (4.0450 Å, ICSD 608628), and $\text{Al}_{60}\text{Cr}_{40}\text{N}$ obtained from DFT calculations in [12,13]. The values of a_0 of the two coatings deposited at $p_{\text{N}_2} = 0.10$ Pa (weak *B*) are within the margin of error of the measurement.

nitrogen pressure increases from 0.08 to 0.3 Pa. Sputtering a thinner target (i.e. higher magnetic flux density *B*) results in a systematically larger a_0 (although rather slightly, by 0.002–0.006 Å) increasing from 4.1136 to 4.1358 Å as the nitrogen pressure increases from 0.1 to 0.2 Pa. Increasing $-U_b$ from 30 to 60 V leads to an increase of a_0 from 4.1205 to 4.1318 Å, followed by a gradual decrease of a_0 to 4.1143 Å upon further increase of $-U_b$ to 150 V. Only the coatings deposited at about 0.1 Pa (the exact pressure is sensitive to the target thickness and bias voltage) have a_0 comparable to that of a defect-free fcc-($\text{Al}_{0.6}\text{Cr}_{0.4}$)N calculated to be 4.114 Å [12,13].

As revealed by the nanoindentation tests, increasing p_{N_2} , *B* (i.e. thinner targets), and $-U_b$, produce a hardening effect (Fig. 4a). This tendency, however, does not apply to the extreme $-U_b$ (150 V) and also

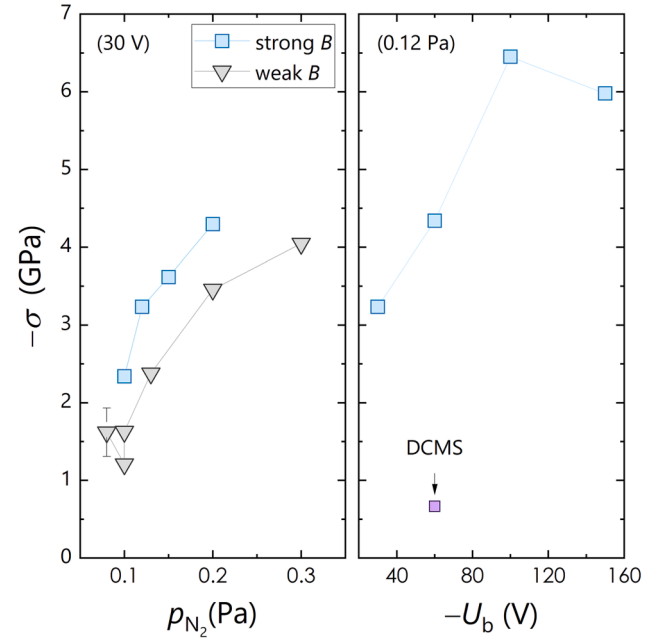


Fig. 5. Compressive residual stresses of the *F*-MS and DCMS (Al,Cr)N coatings.

loses its validity for the lowest p_{N_2} (0.08 Pa). So, increasing p_{N_2} from 0.1 to 0.3 Pa, hardness (*H*) increases from 30.0 ± 1.5 (or 30.5 ± 2.4 in the thicker coating) to 35.7 ± 2.0 GPa. Sputtering a thinner target (i.e. higher *B*) results in a systematically higher *H* (by about 1.5 GPa on average) increasing from 31.6 ± 2.1 to 35.9 ± 4.1 GPa as p_{N_2} increases from 0.1 to 0.2 Pa. Increasing $-U_b$ from 30 to 100 V leads to an increase in *H* from 32.0 ± 4.5 to 37.5 ± 2.7 GPa, followed by a slight softening to 36.4 ± 3.3 GPa upon further increase of $-U_b$ to 150 V. The DCMS (conventional large-area sputtering) and CAE coatings are among the softest showing 29.0 ± 2.1 and 30.2 ± 2.8 GPa, respectively.

The effect of p_{N_2} , $-U_b$, and *B* on Young's modulus (*E*) is slightly less pronounced (Fig. 4b). Upon varying p_{N_2} between 0.1 and 0.3 Pa (irrespective *B*) and $-U_b$ between 30 and 150 V, *E* changes within 460 and 480 GPa, thus being in line with the computational and experimental results on fcc-($\text{Al}_{0.6}\text{Cr}_{0.4}$)N [12,13]. The lowest p_{N_2} used in the study (0.08 Pa at -30 V) results, however, in a substantially smaller *E* value of about 430 GPa, being thus comparable to the DCMS and CAE coatings

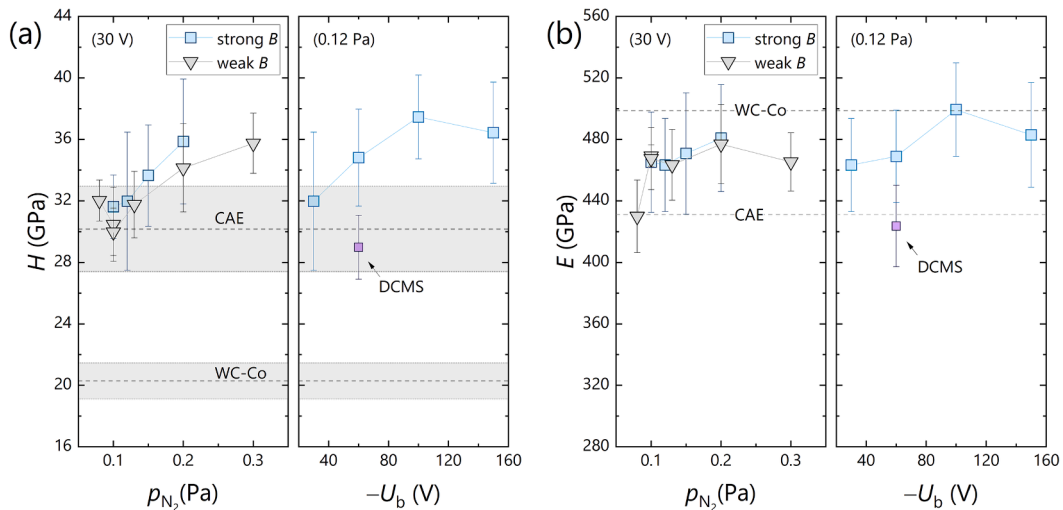


Fig. 4. Nanoindentation hardness (a) and modulus (b) of the *F*-MS (Al,Cr)N coatings as well as the benchmark CAE coating and the substrate WC-Co. In (b), the error bars for the benchmark CAE coating (± 28 GPa) and the substrate (± 26 GPa) are not shown for the sake of clarity.

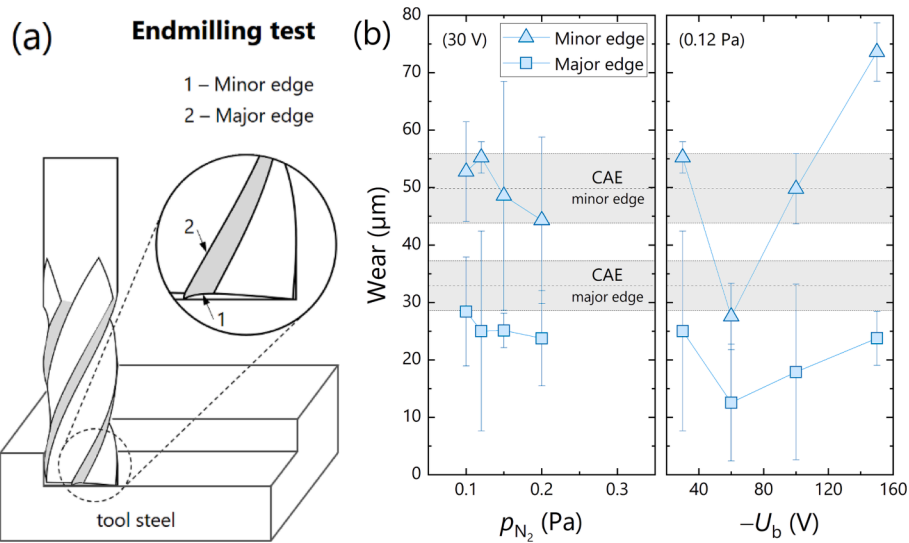


Fig. 6. Schematic illustration of an end milling test (a), mean wear of the major and minor edges of the most relevant *F*-MS coatings in comparison with the performance of the benchmark CAE coating (b).

with 424 and 431 GPa, respectively.

All *F*-MS coatings have compressive residual stresses ($-\sigma$), which increase with the increasing nitrogen pressure, bias voltage, and magnetic field strength (i.e. with decreasing thickness of the target), see Fig. 5. For the lower magnetic field strength, $-\sigma$ increases from 1.2 GPa at 0.1 Pa to 4.0 GPa at 0.3 Pa, while p_{N_2} lower than 0.1 Pa also leads to a higher $-\sigma$ (1.6 GPa). Furthermore, the compressive residual stresses in the near-surface area decrease with increasing thickness, compare the 2.7- and 4.2- μ m-thick coatings deposited at p_{N_2} of 0.1 Pa. For the stronger magnetic field, $-\sigma$ increases from 2.3 GPa at 0.1 Pa to 4.3 GPa at 0.2 Pa. Increasing bias voltage from 30 V to 100 V nearly doubles the compressive residual stresses: compare 3.2 GPa and 6.5 GPa, respectively; whilst a further increase of $-U_b$ to 150 V reduces $-\sigma$ to 6.0 GPa and probably marks a transition to a deposition regime, in which $-U_s$ has the reverse effect on residual stresses.

For the industrial scale cutting tool testing, coatings deposited from the thinned down target (i.e. higher magnetic field strength) were chosen due to the higher hardness. The wear measurements revealed

that the variation of p_{N_2} within the range 0.1–0.2 Pa improves slightly the wear resistance of the end mills coated with the *F*-MS coatings (although with higher nitrogen the accuracy of the measurements does not allow one to make a definite conclusion), which perform as good as the benchmark CAE coating, see Fig. 6. At the same time, bias voltage causes substantial differences in cutting performance. In particular, the end mills coated using $-U_b$ of 60 V (0.12 Pa) show the lowest wear of both major ($13 \pm 10 \mu\text{m}$) and minor ($28 \pm 6 \mu\text{m}$) edges and significantly outperform the benchmark CAE coating with the wear at the major and minor edges being 33 ± 4 and $50 \pm 6 \mu\text{m}$, respectively.

The coating showing the best cutting performance (p_{N_2} of 0.12 Pa and $-U_b$ of 60 V) in the cutting tests was then chosen for the fracture toughness testing by micropillar splitting. The *F*-MS and DCMS coatings exhibit fracture toughnesses (K_{IC}) of 3.80 ± 0.19 and $3.87 \pm 0.26 \text{ MPa}\sqrt{\text{m}}$, respectively (Fig. 7). The benchmark CAE (Al,Cr)N coating has a K_{IC} of $3.73 \pm 0.50 \text{ MPa}\sqrt{\text{m}}$ (on average). The SEM images show the typical fracture of the micropillars for each coating (See Fig. S6 for all images). It is noteworthy that the K_{IC} was effectively the same regardless

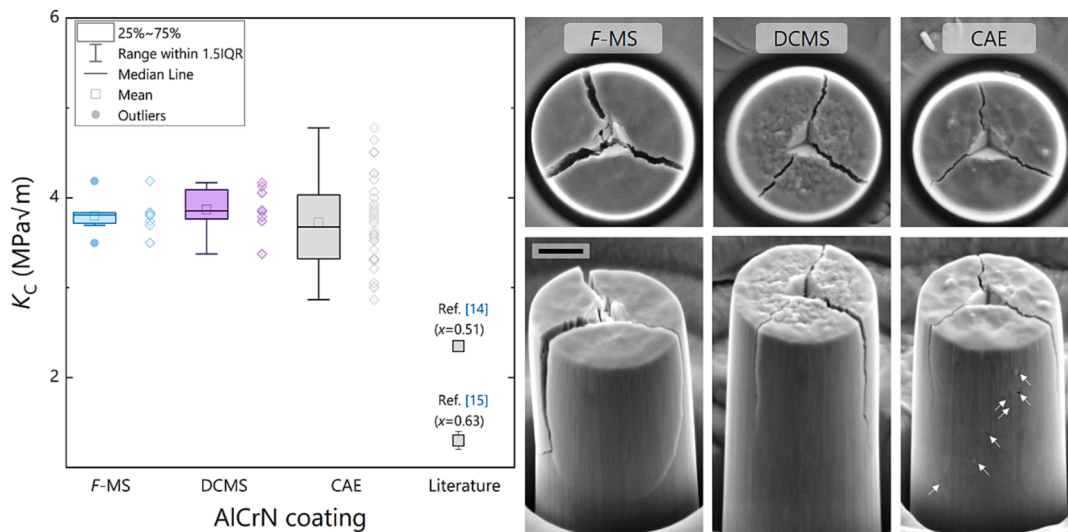


Fig. 7. Fracture toughness of the best performing *F*-MS, DCMS, and benchmark CAE (Al,Cr)N coatings with the K_{IC} values of each individual micropillar shown to the right of the boxes as well as the SEM images of the fractured micropillars (top and side views). The scale bar is 1 μm . The white arrows indicate the growth defects in the micropillars of the CAE benchmark coating visible at the pillar surfaces (a possible reason for the wide spread of K_{IC}). A survey of fracture toughness of $(\text{Al}_x\text{Cr}_{1-x})\text{N}$ coatings, Refs. [14,15].

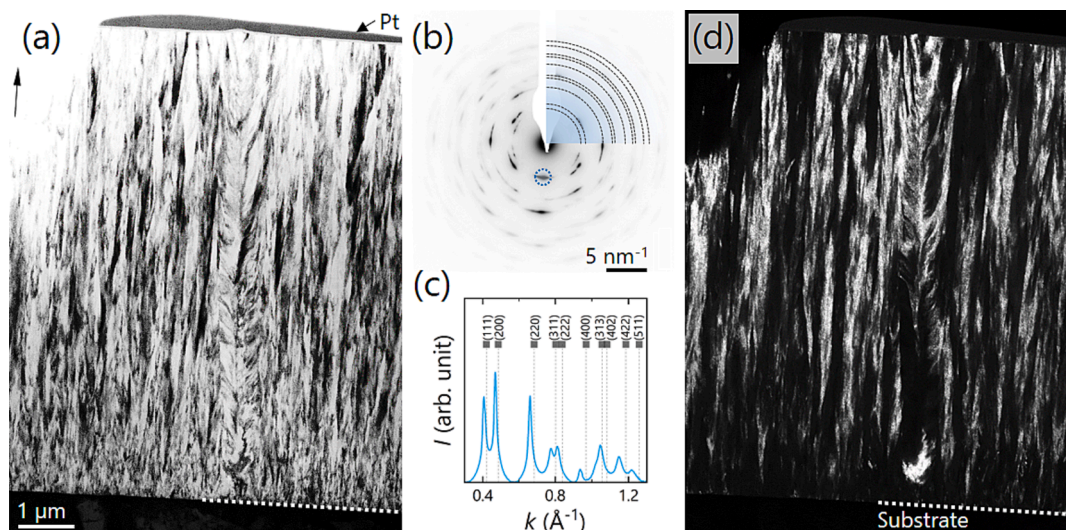


Fig. 8. Microstructure of the *F*-MS coating with the best cutting performance (deposited at 0.12 Pa and -60 V). Bright-field TEM image (a) with the corresponding SAED pattern, (b) radially integrated intensity profile (c) and a dark-field image from the selected spot encircled in (b). The upper left arrow in (a) indicates the direction of growth.

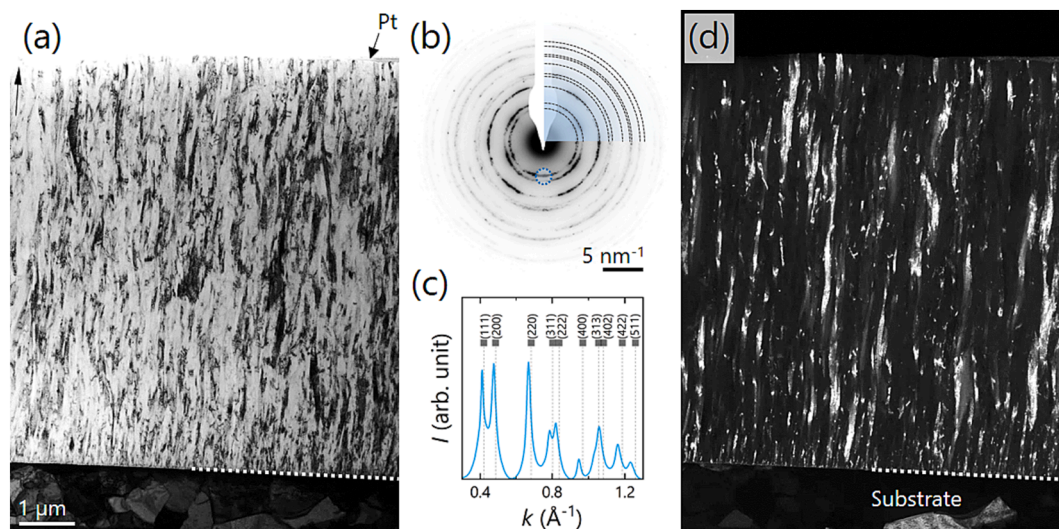


Fig. 9. Microstructure of the DCMS coating deposited under the same condition as the *F*-MS coating with the best cutting performance. Bright-field TEM image (a) with the corresponding SAED pattern, (b) radially integrated intensity profile (c) and a dark-field image from the selected spot encircled in (b). The upper left arrow in (a) indicates the direction of growth.

of whether the pillar underwent a 3-way or a 2-way split upon the initial load drop following maximum load. Additionally, the DCMS coating shows a considerably lower resistance to ion irradiation, which is reflected in over 20% taller micropillars fabricated under similar conditions.

Cross-sectional TEM (XTEM) investigations of the best performing *F*-MS coating as well as DCMS coating deposited using the same conditions are compared in Figs. 8 and 9, respectively. The *F*-MS coating has tightly packed fibrous grains (Fig. 8a). The SAED pattern obtained with a 4- μm aperture centred at the midpoint of the coating confirms that the coatings are single-phase face-centred cubic (Fig. 8b and c). The diffraction in the direction of growth happens primarily on the (111) planes (Fig. 8b) which confirms that the coatings are highly textured. The discrete spots in Fig. 8b are indicative of relatively large grains. Both latter statements are furthermore corroborated by the dark-field XTEM images from a (111) diffraction spot highlighted in Fig. 8d. Similarly, the DCMS coating has a fibrous microstructure (Fig. 9a) and is single-phase face-centred cubic (Fig. 9b and c). However, although the

diffraction in the direction of growth happens also primarily on the (111) planes (Fig. 9b), the intensity is much weaker. The DCMS coating has a more continuous ring pattern and hence a finer grain size. The angular widths of the (111) ring segments of the *F*-MS and DCMS coatings are about 18° and 35° , respectively, thus suggesting a higher degree of mosaicity of the (111) oriented columns of the DCMS coating.

TEM images at higher magnification reveal a completely dense columnar microstructure of the *F*-MS coating and intercolumnar (and minor degree of intracolumnar) porosity can be observed in the DCMS coating (see Fig. 10a and b, respectively). Interestingly, the DCMS coating has a nanolayered structure with a thickness of the individual layers being around 20 nm. STEM EDS (not shown here) revealed slight variations in the Al/(Al + Cr) ratio in the adjacent layers of about 0.02. Furthermore, the grains of the DCMS coating have a wavy shape in the direction of growth (unlike the *F*-MS coating with typical straight grains). It is suggested that these structural peculiarities are caused by a combination of the complex substrate rotation and limited adatom mobility.

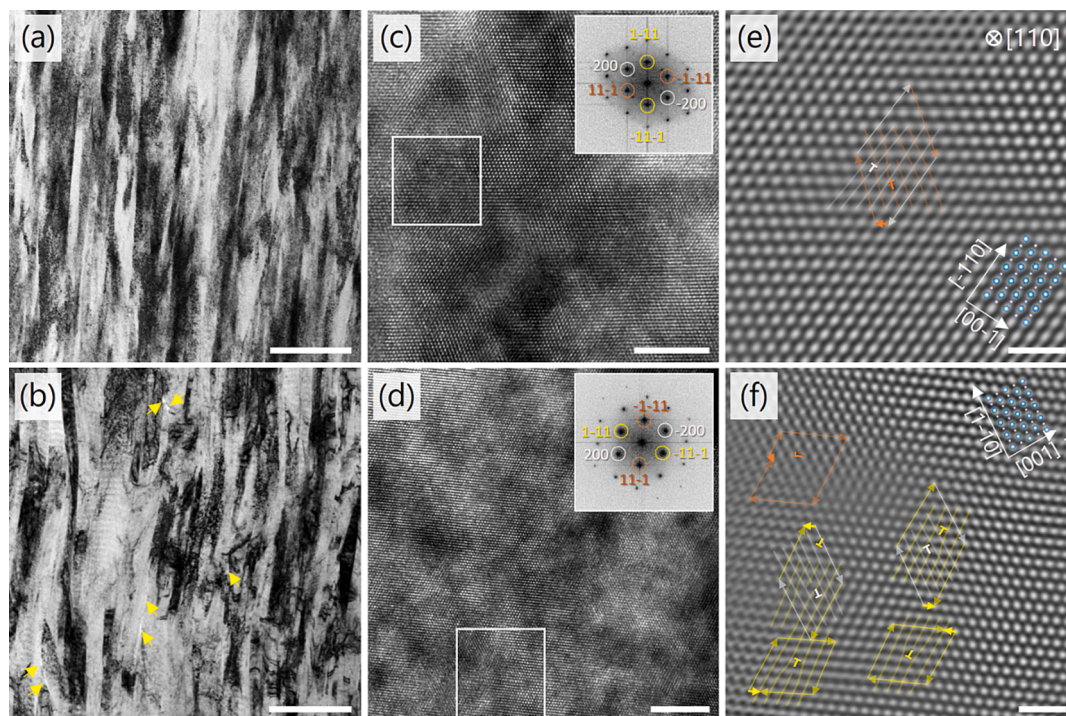


Fig. 10. High-magnification bright-field XTEM (a, b) and Fourier-filtered HRTEM (c–f) of the *F*-MS (top row) and DCMS (bottom row) coatings. Yellow arrows in (a, b) indicate the inter- and intracolumnar pores (the latter can be observed at the top of the image). HRTEM images in (c, d) contains FFT insets and white squares highlighting the areas for selective reconstruction (e, f) by inverse fast Fourier transformation from the spots colour-coded in the FFT insets. The reconstructed HRTEM images show the dislocations (denoted by the symbol “⊥”) with edge components in the $[110]$ zone axis. These were identified from the filtered lattice fringes (see Fig. S7 and S8) and superimposed on the Fourier-filtered HRTEM images. This provides correct numbers but does not show the exact locations of the cores (cf. the locations of the extra half planes in the Lomer locks). The Burgers circuits drawn with the colour-coded arrows demonstrate that some of the dislocations are identified from multiple crystal plane reflectors (e.g. for features consistent with Lomer dislocations). The scale bars are 500 nm in (a, b), 5 nm in (c, d), 1 nm in (e, f). (For interpretation of the references to colour in this figure legend, the reader is referred to the web version of this article.)

Analysis of the high-resolution TEM (HRTEM) images shown in Fig. 10c, d reveals that the *F*-MS coating has a considerably lower density of dislocations as compared to the DCMS coating (see Fig. S9 for the dislocation indicators superimposed on the HRTEM images). Taking into account the sessile Lomer edge dislocations which formed by two extra half planes on the intersecting planes [16,17] (Fig. 10 e, f and Fig. S9), we obtain 7.2×10^{12} and $1.8 \times 10^{13} \text{ cm}^{-2}$, respectively, i.e. relatively high dislocation densities (compare, for instance, to 6.2×10^{12} – $2.2 \times 10^{13} \text{ cm}^{-2}$ in CrN/AlN [18] and 2.4 – 4.7×10^{12} in TiN/AlCrN [15] superlattices). Considering that the areal dislocation density was obtained by counting the dislocations revealed by the (200), (1–11), and (–1–11) reflectors, our figures provide a lower bound on the dislocation density as some dislocation orientations do not give the contrast. The exact slip system cannot be uniquely identified from the Fourier-filtered images (Fig. 10 e, f) acquired along the $[110]$ direction; the commonly observed closure loop vector in the image plane, $a/4[11-2]$, is consistent with the projection of an $a/2[110]$ Burgers vector, where a is the cubic lattice parameter.

Lastly, the microstructure of the benchmark CAE coating has a nanolaminated structure with minor compositional variations due to the use of three targets with different Al/Cr ratios (see Methodology), and planetary rotation of the substrates. Also, microdroplets are ubiquitously distributed throughout the coating along with the voids formed in their vicinity (also visible in the SEM image of the micropillar in Fig. 7).

3. Discussion

Many of our results are coherent with earlier reports on Al–Cr–N coatings. Specifically, higher nitrogen pressure during the deposition process commonly leads to lower Al/(Al + Cr) and higher N/(Al + Cr) ratios [19,20], as well as a higher lattice parameter [21,22], residual

stresses [22,23], hardness [20–22], and Young’s modulus [22], and reduced the wear rate [21]. Also, the effects of bias voltage are extensively studied: upon increasing $-U_b$, Al/(Al + Cr) and N/(Al + Cr) ratios [20,24] and lattice parameter commonly decrease, but residual stresses [22,25], hardness [21,25,26] and Young’s modulus [22] increase, and the wear rate slows down [22]. Too high a bias voltage can negatively affect hardness [20,22].

The effects of the power density on the structure–properties relationship in Al–Cr–N coatings has also been widely studied in the past decade. An increased peak power density in MPP and HiPIMS (corresponds to the DCMS and *F*-MS modes in our study, respectively, see Fig. 1e) causes a denser microstructure and smoother surface, while columnar microstructure is commonly observed in the coatings sputter-deposited at low peak power densities [27–32]. This often leads to a significant enhancement of the mechanical properties in the MPP and HiPIMS coatings [27,31,32]. MPP and HiPIMS coatings also benefit from enhanced coating coverage and adhesion on complex geometries, such as, for instance, cutting tools, as the likelihood of shadowing effects is reduced [27].

The downside of using high peak power densities and hence high degree of ionisation is a phenomenon known as back-attraction of ions to the target resulting in considerably lower deposition rate [30,33]. Using the same deposition parameters, our *F*-MS and DCMS coatings showed the high deposition rates of 2.52 and 2.67 $\mu\text{m/h}$, respectively. (Note that the dark space shield was used in the DCMS mode reducing the deposition rate by a factor of two, see Fig. 1c.) A direct comparison with the results available in literature is, however, problematic because of the strong influence of the deposition conditions (power applied to the targets, partial and total pressure, distance between the target and substrate, etc.). For example, only nitrogen partial pressure varied by 0.1 Pa in the *F*-MS mode resulted in the deposition rates ranging from

1.5 to 3.6 $\mu\text{m}/\text{h}$.

Of particular interest in the current study are thus fracture toughness and cutting performance, which received only little attention previously. However, in order to provide insights into the mechanisms for the mechanical behaviour and wear of the coatings, microstructural peculiarities (including atomic structure and structural defects) need to be elucidated as well. Finally, we also discuss the potential of the novel *F*-MS technology for the coating industry.

3.1. Structure

3.1.1. Atomic structure

All coatings are slightly superstoichiometric and have an Al/(Al + Cr) ratio varying between 0.60 and 0.62, which is considerably below the solubility limit of Al in fcc-(Al,Cr)N being around 0.7 [34,35]. As a result, cubic solid solutions could be stabilised in all *F*-MS (and DCMS) coatings. As p_{N_2} rises, N content in the coatings increases while Al/(Al + Cr) ratio decreases (see Fig. S4). This might be caused by the lower sputtering rates of Al due to its preferential poisoning in the target and incorporation of nitrogen atoms into the lattice (as the lattice expands, too), respectively. By contrast, an increase of $-U_b$ (except 60 V) results in a simultaneous decrease of Al/(Al + Cr) ratio and N content. (This is unlikely to be caused by resputtering as the resputtering rates at bias voltages below 150 V are generally low [36].) Considering the concurrent shrinkage of the crystal lattice upon increasing $-U_b$, it becomes evident that variations of the Al/(Al + Cr) ratio between 0.60 and 0.62 have little effect on the lattice size. In fact, <4 % of the total lattice expansion is due to the reduction of Al content since a decrease of Al content, x , from 0.62 to 0.60 results in a lattice enlargement from 4.1119 to 4.1136 Å [12,13], i.e. by 0.0017 Å whereas the overall lattice enlargement observed in this study is 0.0460 Å. Hence, it is point defects that are primarily responsible for the lattice size variations.

Among such point defects are the interstitial atoms, which form during the deposition process. High ionisation degree of nitrogen in the vicinity of the target results in nitrogen ions being attracted towards the target, which then can be backscattered with high energy by the heavy metal atoms [37] and subsequently subimplanted at the interstitial sites (in the tetrahedral voids, singly or in dimers with 111 split [38]). This idea is corroborated through the series of experiments with a stronger magnetic field (systematically larger lattice parameter), which results in a better confinement of the electrons thus increasing the probability of collisions and ionisation of N_2 and Ar atoms. This leads to higher plasma densities and higher flux of energetic backscattered nitrogen atoms [39]. The concentration of such lattice defects can also be increased through the accelerated N_2^+ . This effect is clearly observed upon increasing bias voltage (and hence ion energy) up to 60 V. Other point defects like Frenkel pairs (i.e., nitrogen atoms dislocated from their original sites to the interstitial sites) can also increase the lattice parameter [40], yet, unlike interstitial atoms, they preserve the stoichiometry. Also Schottky defects, though decreasing the lattice parameter, cannot be ruled out as they generally have a relatively low energy of formation [41–43]. Accordingly, the most plausible hypothesis would be a combination of different point defects with a relatively high concentration of the interstitial atoms. However, since this question is beyond the scope of the current study, we examined this hypothesis separately [44].

3.1.2. Microstructure

The microstructural differences between *F*-MS and DCMS can be understood with the aid of two fundamental parameters, which are often employed in an ion-assisted deposition to control the adatom mobility and nucleation rate (and hence the microstructure) of the metal nitride coatings – ion energy, E_i , and the incident ion-to-metal-atom flux ratio, J_i/J_{Me} [45,46]. Since *F*-MS and DCMS coatings were both deposited under the same conditions, E_i contribution from Ar ions is effectively the same, and hence microstructural differences should arise from the differences in J_i/J_{Me} . Given that in the *F*-MS process higher power densities

result in a higher degree of ionisation of the sputtered particles [47] and thus higher J_i/J_{Me} , the total energy delivered to the *F*-MS coating per deposited atom is considerably higher. Momentum transfer during intense ion bombardment leads to higher nucleation rates and density of the coatings [48,49].

A distinct difference of the DCMS coating is that the disruption of the local epitaxial growth and renucleation occur more frequently. Its microstructure is furthermore characterised by intercolumnar porosity (and even intracolumnar voids, although with a much smaller volume fraction) due to limited surface diffusion, which is indicative of a low-energy, low-flux ion irradiation [48]. (Although controlling E_i can densify the microstructure at low J_i/J_{Me} , there is only a narrow interval of the ion energies leading to densification without substantial radiation damage and subimplantation [48].) Similar observations were made by Leroy et al. who compared HiPIMS and DCMS by sputtering a laboratory-scale tubular target [50,51]. Energy flux per deposited atom is up to several times higher for HiPIMS, irrespective of whether sputtering is happening in metallic or “poisoned” regime [51]. Finally, the lower ion-to-metallic-atom ratio and resulting limited surface diffusion may have resulted in higher dislocation density and, combined with the deposition geometry (rotation of the substrates and different angular distribution functions of the Al and Cr), nanolayered structure of the DCMS coating.

3.2. Mechanical properties

3.2.1. Nanoindentation hardness and modulus

As seen in the previous section, upon increasing nitrogen pressure, magnetic field strength (i.e. thinner targets), or bias voltage, the concentration of defects exerting strains on the surrounding lattice increases. The lattice strain fields in turn provide impediments to dislocation motion resulting in strengthening and hardening [52–54]. In particular, higher nitrogen pressure and stronger magnetic field result in higher concentration of nitrogen atoms occupying interstitial sites and ultimately in higher hardness of the coating (Fig. 4a). (Too low nitrogen pressures might however favour the formation of vacancies on the nitrogen sublattice, which can also exert strains on the surrounding lattice and impede dislocation motion and increase hardness [55].) Similarly, high defect density and hence hardness can be achieved by increasing bias voltage (Fig. 4b). For excessively high bias voltage, however, the tendency no longer holds true and a detrimental effect on hardness is commonly observed [20,26]. A possible reason is that too high a bias voltage and hence energy of the accelerated ions can reduce the amount of point defects, akin to the annihilation of Frenkel pairs in (V,Al)N [56].

For the grain boundaries (GBs) to inhibit the flow of dislocations, they have to be fully dense as micropores will act as stress concentrators and have detrimental effect on strength and hardness [52,57]. Stronger magnetic field can have a beneficial effect as higher flux of the backscattered Ar atoms, which, unless fully thermalised, can increase the density of the growing coating through the momentum transfer. Significantly more efficient is, however, to apply bias voltage and attract energetic Ar ions [58]. Despite using the similar deposition conditions, the DCMS coating grew with intergranular and, though to a much lesser extent, intragranular porosity (Fig. 11) and substantially lower hardness than the *F*-MS coating (Fig. 4a). The reason is, as described in the previous section, considerably lower ionisation degree of the sputtered particles and the total energy delivered to the coating per deposited atom. Due to the inability to increase the incident flux ratio J_i/J_{Me} in the DCMS process, higher densities and hence hardness of the coatings can be achieved by applying higher bias voltage. In TiN, for instance, densification of the microstructure was observed for $-U_b$ above 120 V [58].

The effect of the deposition condition (nitrogen pressure, magnetic field strength, and bias voltage) on Young's modulus of the *F*-MS coatings is modest, resulting in variation within the range 460–480 GPa. This suggests only small changes in the density and bonding character upon

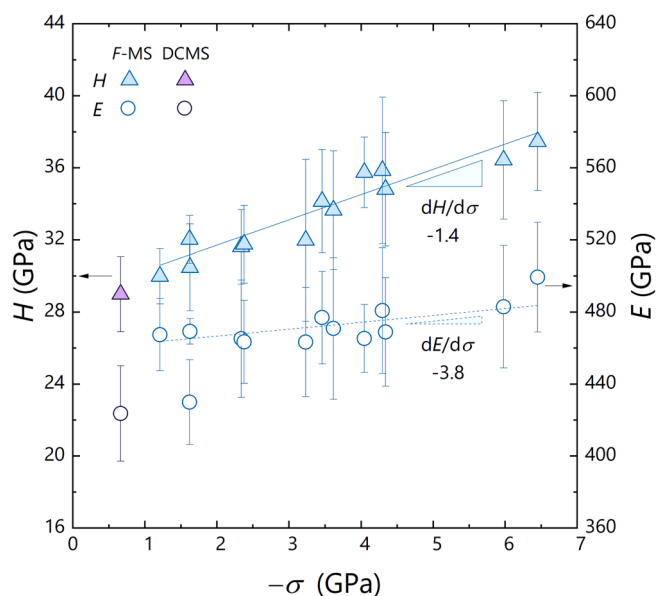


Fig. 11. Correlation between hardness (left axis) or Young's modulus (right axis) and residual stresses.

increasing the defect concentration. The lowest p_{N_2} (0.08 Pa at -30 V) used in the *F*-MS study results, however, in considerably smaller E of 430 ± 24 , which can be caused by the formation of vacancies as has been shown for metal nitrides [59]. The DCMS coating has a similar Young's modulus, yet this seems to be caused by the microporosity (Fig. 10).

Grain size appears to play a subordinate role in hardness and Young's modulus. So, for instance, when comparing the line broadening for the (111) reflections (Fig. S2b), coatings deposited using the stronger magnetic field show lower full width at half maximum (FWHM) values, thus suggesting a larger size of the scattering domains. At the same time, higher hardness is consistently measured for this series of coatings. Similarly, smaller grains should decrease the Young's modulus [60]. Although this seems to provide reasonable explanation for the coating deposited using the lowest nitrogen pressure showing a noticeably greater FWHM value (Fig. S2b) and thus a smaller size of the coherently scattering domains, the coating with by far the highest FWHM value (1°) and the coatings with FWHM in the range 0.2 – 0.3° have similar Young's moduli. Hence, a much greater impact can be ascribed to other effects, e. g. porosity [60].

3.2.2. Residual stress

As shown in Fig. 11, hardness shows a pronounced correlation with the residual stresses with $dH/d(-\sigma)$ of 1.4 ± 0.2 (in other words, increase of $-\sigma$ by 1 GPa coincides with an increase of H by 1.4 GPa); the same correlation is observed in other nitride coatings [61]. Hardness is often observed to correlate with residual stresses in CrAlN [62] and coatings produced by means of physical vapour deposition (PVD) in general [63–66]. The correlation between Young's modulus and residual stresses is much less pronounced with $dE/d(-\sigma)$ of 3.8 ± 2.2 (in other words, increase of $-\sigma$ by 1 GPa coincides with an increase of E by 3.8 GPa) but can be several times higher, compare, for instance, TiAlN coatings with $dE/d(-\sigma)$ of 11.6 [67].

The residual stresses in the coatings form primarily during the deposition process due to the microstructural and chemical defects (i.e. intrinsic stresses) and upon cooling from the deposition temperature due to the mismatch of the thermal expansion coefficients between coating and substrate [68–74]. Given that the small compositional variations in fcc-(Al_{0.6}Cr_{0.4})N have a negligible effect on the thermal expansion coefficient [75], residual stresses appear to be governed by the intrinsic stresses. As pointed out above, the intrinsic stresses are cumulated by microstructural and chemical defects which in turn can be, for instance,

nitrogen atoms occupying the interstitial lattice sites (variation of p_{N_2}) or other point defects (e.g. Frenkel pairs [76]) but also line defects (variation of $-U_b$). The lower compressive stresses in the DCMS coating are likely to be due to the reduced density of the GBs allowing the stresses generated during the deposition process to relax [77] as well as the formation of dislocation dipoles (cf. Figs. S7 and S8) being favourable for strain relaxation.

3.2.3. Fracture toughness

Residual stresses inevitably influence fracture toughness of the coatings. When assessing the fracture toughness using the nano-indentation cracking technique [78,79], apparent fracture toughness is observed to be dependent on the residual stresses [80]. (Although compressive residual stresses are effective in counteracting the stresses and strains experienced at the crack tip and hence in impeding crack, the structural integrity of the coating depends greatly on the strength of the grain boundaries [81].) To assess the intrinsic fracture toughness, the residual stresses have to be released. This can be achieved, for instance, in micropillar splitting testing, provided that the height of the micropillar is greater than its diameter (that is aspect ratio greater than 1) [82]. In the current study, both sputter-deposited coatings, *F*-MS and DCMS coatings, have relatively high fracture toughness with K_C of 3.80 ± 0.19 and 3.87 ± 0.26 MPa \sqrt{m} , respectively (Fig. 6), which reach and even exceed K_C of the benchmark CAE coating being 3.73 ± 0.50 MPa \sqrt{m} .

Generally, ceramic materials such as metal nitrides are inherently brittle at low temperatures due to the ease of crack nucleation and propagation. The former is due to the pre-existing micropores, which are the locations of the highest stress concentration, while the latter is due to a lack of appreciable plastic dissipation. If the microstructure is fully dense, plastic deformation in a ceramic material with a face-centred cubic structure primarily occurs by dislocation movement on the {111} or {110} planes (largely depending on the ionic contribution to the bonding, loading direction, temperature) along $\langle 1-10 \rangle$ or $\langle 11-2 \rangle$ direction with the Peierls stress acting as the rate governing mechanism [17,52]. In the PVD coatings, however, fracture commonly occurs along the GBs which have a lower fracture resistance than the grain interior [83–85]. Accordingly, cracks in the coatings with columnar microstructure would traverse the entire thickness. Engineering the GBs to enable crack deflection or hinder crack propagation is an effective mechanism for energy dissipation [86,87]. It is widely used to improve fracture toughness, for instance, by activating delamination toughening [88], twisting and tilting columnar grains [89–92], in multilayer and superlattices [93–95], and combination thereof [96].

In fact, the relatively high K_C values of the CAE and DCMS coatings are believed to be due primarily to their microstructure composed of many few-nm-thin layers with varying Al/(Al + Cr) ratios. Such compositional oscillations cause lattice mismatch and thus coherency stains along the interfaces. In addition, markedly higher dislocation densities in the DCMS coating (as compared to the *F*-MS coating) can improve toughness by dislocation motion before crack growth [97]. At the same time, voids forming in the vicinity of the microdroplets, which can reach several tens of nanometres in size (Fig. 7), act as stress raisers and can initiate a crack. As the probability of the existence of a void or void volume fraction varies from micropillar to micropillar, the wide spread of the K_C values for the CAE coating appears reasonable. It also suggests that a substantial improvement of fracture toughness can be achieved if the void formation is prevented.

Comparing the fracture toughness of our (Al,Cr)N coatings with CrN having 2.95 ± 0.23 MPa \sqrt{m} (as determined by means of micropillar splitting tests) [98], an addition of aluminium results in solid solution toughening by 29% (*F*-MS), 31% (DCMS), and 26% (CAE). An addition of a similar amount of Al to TiN, that is 60% on the metal sublattice, results in a comparable 42% increase of fracture toughness from 1.9 to 2.7 MPa \sqrt{m} [99]. Since this is the first report on fracture toughness of (Al,Cr)N coatings carried out by means of micropillar splitting tests, we

cannot compare our results directly to the available results on (Al,Cr)N coatings. However, fracture toughness by means of cantilever bending test (K_{IC}) was assessed in several recent studies on sputter-deposited (Al_xCr_{1-x})N coatings. The values range from 2.35 MPa \sqrt{m} ($x = 0.51$, A. Drnovšek et al. [14]) to 1.3 MPa \sqrt{m} ($x = 0.63$, J. Buchinger et al. [15]). When attempting to draw a comparison between the results, it is important to keep in mind that fracture toughness determined in a single cantilever bending test is likely to be influenced by Ga^+ ions sub-implanted in the notch during the FIB milling process. In micropillar splitting tests, by contrast, the initial sub-critical cracks generate in a region being largely unaffected by the FIB milling process. In a comparative study on CrN coatings [98], fracture toughness determined in a single cantilever bending test was found to be systematically higher than in micropillar splitting tests. Accordingly, our coatings have, presumably, higher fracture toughness than any other sputter-deposited (Al,Cr)N coatings investigated previously. This might be possible because of higher cohesive energy of the columnar GBs resulting from the deposition process developed in this study. Finally, optimising F -MS processing conditions to match the DCMS dislocation content is envisioned to further improve toughness.

3.3. Cutting performance

In cutting tests, coatings deposited using high nitrogen pressures have previously been shown to result in lower wear rates [21]. A similar observation has been made in this study (Fig. 6b). As discussed above, higher nitrogen pressure during the deposition results in higher compressive residual stresses. This can improve fracture toughness, as compressive residual stresses can mitigate the stresses and strains arising at the crack tip and thus impede crack propagation. When comparing the F -MS and DCMS coatings having rather similar stress-free fracture toughness values (the mean value is 6% higher for the DCMS coating), the F -MS coating can be expected to show a substantially higher resistance to crack propagation with the compressive residual stresses being more than 6 times higher than in the DCMS coating (compare $-\sigma = 4.3$ GPa and 0.7 GPa, respectively). Also, the F -MS coating is the hardest with H of 34.8 ± 3.2 GPa (17% and 13% harder than DCMS and CAE, respectively), so the highest resistance against abrasive wear was anticipated. However, the results of the cutting tests show that both the F -MS and DCMS coatings are equally effective in prolonging the tool life and both outperform the benchmark CAE coating.

The semi-empirical criteria H/E (elastic strain to failure [100]) and H^3/E^2 (resistance to plastic deformation [101]) are often used to predict fracture toughness and wear resistance of the coatings [100,102]. Besides the relative simplicity in their assessment, these criteria can also account for the residual stresses (if nanoindentation testing is performed on the coated tool since residual stresses depend on the substrate material [103]). However, it has been shown that both criteria can lose their predictive power upon substantial changes of the microstructure [104,105]. In this study, F -MS, DCMS, and CAE coatings have H/E of 0.07 ± 0.01 , 0.07 ± 0.01 , 0.07 ± 0.01 , and H^3/E^2 of 0.19 ± 0.02 GPa, 0.14 ± 0.02 GPa, 0.15 ± 0.02 GPa, respectively. This implies the best wear resistance of the F -MS coating, while rather similar results for the DCMS and CAE coatings. In other words, the semi-empirical criteria cannot explain the good wear resistance of the DCMS coating in the cutting tests.

Besides abrasive wear, other fundamental mechanisms play an important role in the overall performance of the coating. These can include adhesion with the substrate and the chip from the work piece. The F -MS coatings have a considerably lower fraction of growth defects as compared to the DCMS and CAE coatings. Smoother surfaces commonly result in a lower wear rate [1,106]. The F -MS coating has a density comparable to that of the CAE coating, while the DCMS coating forms with the porous grain boundaries. This detrimentally affects not only the mechanical properties, but ultimately facilitates the inward diffusion of oxygen under the operating conditions, too. Besides,

microstructure and elemental concentration and thus properties of the coating directly at the cutting edge and far from the edge where the measurements are commonly carried out (as here) can substantially vary [107,108]. Additionally, under conditions of interrupted cutting (e.g., end milling operations), elevated temperatures as well as thermal shock due to the temperature fluctuations and the cyclic impact can decisively affect the performance of the coatings.

Therefore, given the complexity of the wear mechanisms being activated during the cutting tests, the semi-empirical criteria based on the room-temperature hardness, Young's modulus, and fracture toughness might quickly lose their predictive power for the wear resistance. Hence, further investigations at cutting temperatures and loading conditions at the cutting edges are needed in order to link the performance of a wear-resistant coating with its properties.

4. Conclusions

A novel technology allowing one to sputter industrial-size tubular targets at high-plasma power densities (F -MS) has been developed. This is achieved by a longitudinal movement of the magnetron inside the target. To assess the quality and performance of the F -MS coatings, we first optimised the process parameters by sputtering an $Al_{60}Cr_{40}$ target using different nitrogen pressures, bias voltages, and (though indirectly) strengths of magnetic field. All coatings were single-phase with a face-centred cubic structure and (111) preferential orientation, fully dense microstructure, and much lower volume fraction of the growth defects and surface roughness than in the benchmark coating produced by means of cathodic arc evaporation (CAE). Despite similar toughness values, the F -MS coatings show up to 150 % better wear resistance than the benchmark CAE coating. These outstanding results, along with the potential for further improvement through microstructural design, attest great capabilities of this technology in producing wear-resistant coatings for advanced engineering applications.

5. Methodology

The benchmark CAE (Al_xCr_{1-x})N coatings were deposited on rotating substrates (3-fold rotation) at 480 °C by simultaneously evaporating three alloyed tubular targets $Al_{70}Cr_{30}$, $Al_{55}Cr_{45}$, and $Al_{70}Cr_{30}$ (99.95% purity, Ø110x510 mm, PLANSEE Composite Materials GmbH, Germany) in a π 411 industrial PVD unit (PLATIT AG, Switzerland) in a nitrogen atmosphere, using a process pressure of 3.8 Pa, and a bias voltage of -40 V during the first third of the deposition process, followed by -180 V for the remaining duration.

The F -MS coatings were deposited in a π 411 industrial PVD unit (PLATIT a.s., Czech Republic) from an $Al_{60}Cr_{40}$ rotating tubular target (99.95% purity, Ø110x510 mm, PLANSEE Composite Materials GmbH, Germany), with a magnetron moving longitudinally inside (see Fig. 1c), at 480 °C and Ar pressure of 0.27 Pa. By using a DC power supply with a total output power of 25 kW, three series of coatings were produced. Two series were produced at different nitrogen pressures applying a bias voltage of -30 V. Here, one series was produced from a pristine target, another – after extensive use of the target, hence from a substantially thinner target. In doing so, we were aiming at investigating the effect of the magnetic field strength (the thinner the target the stronger the magnetic field [39,109]). Here, the magnetic field strength increased from 51 ± 1 mT in the first series up to 72 ± 4 mT in the second, constituting an approximate 40% increase). The third series of the (Al, Cr)N coatings was produced by changing the bias voltage from -30 V to -150 V. For comparison, the deposition conditions used for the F -MS coating performing best in cutting tests (25 kW DC power supply, 0.12 Pa process pressure, -60 V bias voltage) were used to deposit a coating with a conventional magnetron inside of the same $Al_{60}Cr_{40}$ rotating tubular target (which is referred to as DCMS in the current article, see Fig. 1c).

Due to the planetary rotation of the substrates, the distance between

the substrates and the target varied between 6 and 18 cm. For microstructural investigations and nanoindentation tests, coatings with a thickness of about 3.5 μm were deposited on WC-Co (SANDVIK Grade H10F, 10 mol. % Co) substrates. For micromechanical studies, much thicker coatings (between 8 and 10 μm) were deposited on Co-free WC substrates (PLANSEE Composite Materials GmbH, Germany).

Bragg-Brentano X-ray diffraction (BBXRD) of monochromised $\text{CuK}\alpha$ radiation ($\lambda = 1.5406 \text{ \AA}$) was used to gain information about the phase composition and preferential orientation, while glancing angle XRD (GAXRD) with an incident angle γ of 3° was used to assess the phase composition, stress-free lattice parameter, and residual stress of the cubic phase based on a modified $\sin^2\psi$ method [110]. Chemical composition by energy dispersive X-ray spectroscopy (EDS), which was calibrated using a CrN standard (Ardennes Analytique Hungary Kft). A detailed transmission electron microscopy (TEM) of focused ion beam (FIB) prepared liftouts, using bright- and dark-field STEM imaging, and small-area chemical mapping by STEM-EDX.

Nanoindentation analysis was carried out using a quasi-continuous stiffness measurement (QCSM) technique (ZwickRoell). Here, the applied force is increased in steps and a sinusoidal oscillation is superimposed on the Piezo voltage. Besides, two reference samples with distinctly different elastic moduli were used for the area tip and compliance calibration as described in detail in Ref. [111]. These materials are SiO_2 ($E = 72 \text{ GPa}$, $\nu = 0.17$) and Al_2O_3 ($E = 410 \text{ GPa}$, $\nu = 0.234$). Indentation hardness, H , and modulus, E , of our thin films were then obtained by evaluating the load–displacement curves of nanoindentation tests (Berkovich diamond tip and the loads up to 100 mN) after Oliver and Pharr [112] and as described in detail by A.C. Fischer-Cripps [113]. A subsequent test on Al_2O_3 yields H of $24.9 \pm 2.0 \text{ GPa}$ and E of $413 \pm 16 \text{ GPa}$ (and comparable $25.4 \pm 1.9 \text{ GPa}$ and E of $395 \pm 15 \text{ GPa}$ when the tip area calibration is done using solely SiO_2), thus providing a lower bound of the previously reported values [111,112,114]. A Poisson's ratio of fcc-($\text{Al}_x\text{Cr}_{1-x}$)N show only minor departures from 0.2 for x within the range 0.54–0.63 as follows from the calculations based on the density functional theory [13].

Fracture toughness was assessed using micropillar splitting technique [115]. The micropillars were fabricated using a focused ion beam (FIB, Tescan, Czech Republic) in a two-step process. The rough milling to 5 μm diameter was performed at about 4 nA, while polishing down to about 3 μm was done at about 200 pA. In-SEM micropillar splitting tests were carried out using a nanoindenter (Alemnis AG, Switzerland) in displacement-controlled mode using a cube-corner tip (Synton AG, Switzerland). The critical load before the fracture is reached, P_C , was used together with the radius of the pillars, R , to assess fracture toughness, K_C :

$$K_C = \gamma \frac{P_C}{R^{3/2}}$$

with γ being a coefficient depending on the indenter tip geometry as well as hardness and Young's modulus of the coating [116] (See Fig. S5 for more information).

To evaluate the cutting performance of the coatings in real working conditions, dry trochoidal milling tests were carried out according to ISO 8688 (Fehlmann Picomax 60-M, Fehlmann AG, Switzerland). End mills (MB-NVDS, Fraisa AG, Switzerland) coated with the selected coatings were used to machine AISI P20 + S tool steel (HRC 28) with the following composition: 0.40 wt% C, 0.40 wt% Si, 1.50 wt% Mn, 1.90 wt % Cr, 0.20 wt% Mo, 0.06 wt% S. Cutting speed and feed rate per tooth were set to 177 m/min and 0.179 mm/rev., respectively. The radial and axial cutting depths were 0.6 and 10 mm, respectively. The total wear was evaluated after removing 2500 cm^3 of the tool steel.

CRedit authorship contribution statement

F.F. Klimashin: Investigation, Methodology, Writing – original

draft, Writing – review & editing, Data curation. J. Kluson: Investigation, Methodology, Writing – review & editing, Data curation. M. Učík: Investigation, Methodology, Writing – review & editing, Data curation. R. Žemlička: Investigation, Methodology, Writing – review & editing, Data curation. M. Jílek: Methodology, Writing – review & editing. A. Lümkmann: Writing – review & editing, Supervision, Resources, Project administration. J. Michler: Writing – review & editing, Supervision, Resources, Project administration. T.E.J. Edwards: Investigation, Writing – review & editing, Supervision, Resources, Project administration.

Declaration of Competing Interest

The authors declare that they have no known competing financial interests or personal relationships that could have appeared to influence the work reported in this paper.

Data availability

Data will be made available on request.

Acknowledgments

This research was supported by the Innosuisse Project 42220.1 IP-ENG. The authors thank Dr. Krzysztof Wieczerzak and Dr. Remo Widmer for experimental assistance in the initial stage of the study.

Appendix A. Supplementary data

Supplementary data to this article can be found online at <https://doi.org/10.1016/j.matdes.2023.112553>.

References

- [1] M. Tkadletz, C. Mitterer, B. Sartory, I. Letofsky-Papst, C. Czettel, C. Michotte, The effect of droplets in arc evaporated TiAlTaN hard coatings on the wear behavior, *Surf. Coat. Technol.* 257 (2014) 95–101.
- [2] V. Kouznetsov, K. Macak, J.M. Schneider, U. Helmersson, I. Petrov, A novel pulsed magnetron sputter technique utilizing very high target power densities, *Surf. Coat. Technol.* 122 (2–3) (1999) 290–293.
- [3] J. Gudmundsson, N. Brenning, D. Lundin, U. Helmersson, High power impulse magnetron sputtering discharge, *J. Vac. Sci. Technol. A* 30 (3) (2012).
- [4] J.E. Greene, Tracing the recorded history of thin-film sputter deposition: From the 1800s to 2017, *J. Vac. Sci. Technol. A* 35 (5) (2017), 05C204.
- [5] R. De Gryse, J. Haemers, W. Leroy, D. Depla, Thirty years of rotatable magnetrons, *Thin Solid Films* 520 (18) (2012) 5833–5845.
- [6] O. Knotek, M. Atzor, A. Barimani, F. Jungblut, Development of low temperature ternary coatings for high wear resistance, *Surf. Coat. Technol.* 42 (1) (1990) 21–28.
- [7] S. Hofmann, H. Jehn, Oxidation behavior of CrNx and (Cr, Al) Nx hard coatings, *Mater. Corros.* 41 (12) (1990) 756–760.
- [8] O. Knotek, F. Löffler, H.J. Scholl, Properties of Arc-Evaporated Crn and (Cr, Al)N Coatings, *Surf. Coat. Technol.* 45 (1–3) (1991) 53–58.
- [9] K. Bobzin, E. Lugscheider, R. Nickel, P. Immich, (Cr1-x, Alx) N ein Review über ein vielseitig einsetzbares Schichtsystem, *Materialwissenschaft und Werkstofftechnik: Entwicklung, Fertigung, Prüfung, Eigenschaften und Anwendungen technischer Werkstoffe* 37 (10) (2006) 833–841.
- [10] K. Bobzin, High-performance coatings for cutting tools, *CIRP J. Manuf. Sci. Technol.* 18 (2017) 1–9.
- [11] J. Vetter, A.O. Eriksson, A. Reiter, V. Derflinger, W. Kalss, Quo vadis: Alcr-based coatings in industrial applications, *Coatings* 11 (3) (2021) 344.
- [12] P.H. Mayrhofer, D. Music, T. Reeswinkel, H.G. Fuß, J.M. Schneider, Structure, elastic properties and phase stability of Cr1-xAlxN, *Acta Mater.* 56 (11) (2008) 2469–2475.
- [13] L. Zhou, D. Holec, P.H. Mayrhofer, First-principles study of elastic properties of cubic Cr1-xAlxN alloys, *J. Appl. Phys.* 113 (4) (2013), 043511.
- [14] A. Drnovšek, H.T. Vo, M.R. de Figueiredo, S. Kolozsvári, P. Hosemann, R. Franz, High temperature fracture toughness of single-layer CrAlN and CrAlSiN hard coatings, *Surf. Coat. Technol.* 409 (2021), 126909.
- [15] J. Buchinger, A. Wagner, Z. Chen, Z. Zhang, D. Holec, P.H. Mayrhofer, M. Bartosik, Fracture toughness trends of modulus-matched TiN/(Cr, Al) N thin film superlattices, *Acta Mater.* 202 (2021) 376–386.
- [16] L. Wang, X. Han, P. Liu, Y. Yue, Z. Zhang, E. Ma, In situ observation of dislocation behavior in nanometer grains, *Phys. Rev. Lett.* 105 (13) (2010), 135501.
- [17] J. Salamaia, D. Sangiovanni, A. Kraych, K.C. Kwick, I. Schramm, L. Johnson, R. Boyd, B. Bakhit, T. Hsu, M. Mrovec, Elucidating dislocation core structures in

- titanium nitride through high-resolution imaging and atomistic simulations, *Mater. Des.* 224 (2022), 111327.
- [18] X. Gu, Z. Zhang, M. Bartosik, P.H. Mayrhofer, H. Duan, Dislocation densities and alternating strain fields in CrN/AlN nanolayers, *Thin Solid Films* 638 (2017) 189–200.
 - [19] R. Wuhner, W. Yeung, A comparative study of magnetron co-sputtered nanocrystalline titanium aluminium and chromium aluminium nitride coatings, *Scr. Mater.* 50 (12) (2004) 1461–1466.
 - [20] L. Wang, S. Zhang, Z. Chen, J. Li, M. Li, Influence of deposition parameters on hard Cr–Al–N coatings deposited by multi-arc ion plating, *Appl. Surf. Sci.* 258 (8) (2012) 3629–3636.
 - [21] B. Warcholinski, A. Gilewicz, P. Myslinski, E. Dobruchowska, D. Murzynski, Structure and properties of AlCrN coatings deposited using cathodic arc evaporation, *Coatings* 10 (8) (2020) 793.
 - [22] J.-F. Tang, C.-Y. Lin, F.-C. Yang, C.-L. Chang, Influence of nitrogen content and bias voltage on residual stress and the tribological and mechanical properties of CrAlN films, *Coatings* 10 (6) (2020) 546.
 - [23] F. Lomello, F. Sanchette, F. Schuster, M. Tabarant, A. Billard, Influence of bias voltage on properties of AlCrN coatings prepared by cathodic arc deposition, *Surf. Coat. Technol.* 224 (2013) 77–81.
 - [24] J. Romero, M. Gómez, J. Esteve, F. Montalà, L. Carreras, M. Grifol, A. Lousa, CrAlN coatings deposited by cathodic arc evaporation at different substrate bias, *Thin Solid Films* 515 (1) (2006) 113–117.
 - [25] Y.X. Wang, S. Zhang, J.-W. Lee, W.S. Lew, B. Li, Influence of bias voltage on the hardness and toughness of CrAlN coatings via magnetron sputtering, *Surf. Coat. Technol.* 206 (24) (2012) 5103–5107.
 - [26] C. Sabetz, J. Paulitsch, S. Kolozsvári, R. Rachbauer, P. Mayrhofer, Influence of bias potential and layer arrangement on structure and mechanical properties of arc evaporated Al–Cr–N coatings, *Vacuum* 106 (2014) 49–52.
 - [27] K. Bobzin, N. Bagcivan, P. Immich, S. Bolz, R. Cremer, T. Leyendecker, Mechanical properties and oxidation behaviour of (Al, Cr) N and (Al, Cr, Si) N coatings for cutting tools deposited by HPPMS, *Thin Solid Films* 517 (3) (2008) 1251–1256.
 - [28] N. Bagcivan, K. Bobzin, S. Theiß, (Cr1 – xAlx) N: a comparison of direct current, middle frequency pulsed and high power pulsed magnetron sputtering for injection molding components, *Thin Solid Films* 528 (2013) 180–186.
 - [29] C. Kunze, R.H. Brugnara, N. Bagcivan, K. Bobzin, G. Grundmeier, Surface chemistry of PVD (Cr, Al) N coatings deposited by means of direct current and high power pulsed magnetron sputtering, *Surf. Interface Anal.* 45 (13) (2013) 1884–1892.
 - [30] N. Bagcivan, K. Bobzin, G. Grundmeier, M. Wiesing, O. Ozcan, C. Kunze, R. Brugnara, Influence of HPPMS pulse length and inert gas mixture on the properties of (Cr, Al) N coatings, *Thin Solid Films* 549 (2013) 192–198.
 - [31] Y.-C. Hsiao, J.-W. Lee, Y.-C. Yang, B.-S. Lou, Effects of duty cycle and pulse frequency on the fabrication of AlCrN thin films deposited by high power impulse magnetron sputtering, *Thin Solid Films* 549 (2013) 281–291.
 - [32] K. Bobzin, T. Brögelmann, N. Kruppe, M. Engels, Influence of dcMS and HPPMS in a dcMS/HPPMS hybrid process on plasma and coating properties, *Thin Solid Films* 620 (2016) 188–196.
 - [33] G. Greczynski, L. Hultman, Peak amplitude of target current determines deposition rate loss during high power pulsed magnetron sputtering, *Vacuum* 124 (2016) 1–4.
 - [34] A. Reiter, V. Derflinger, B. Hanselmann, T. Bachmann, B. Sartory, Investigation of the properties of Al 1–x Cr x N coatings prepared by cathodic arc evaporation, *Surf. Coat. Technol.* 200 (7) (2005) 2114–2122.
 - [35] P.H. Mayrhofer, H. Willmann, A.E. Reiter, Structure and phase evolution of Cr–Al–N coatings during annealing, *Surf. Coat. Technol.* 202 (20) (2008) 4935–4938.
 - [36] I. Petrov, L. Hultman, J.E. Sundgren, J. Greene, Polycrystalline TiN films deposited by reactive bias magnetron sputtering: Effects of ion bombardment on resputtering rates, film composition, and microstructure, *J. Vac. Sci. Technol. A* 10 (2) (1992) 265–272.
 - [37] K. Sarakinos, J. Alami, P. Karimi, D. Severin, M. Wuttig, The role of backscattered energetic atoms in film growth in reactive magnetron sputtering of chromium nitride, *J. Phys. D Appl. Phys.* 40 (3) (2007) 778.
 - [38] E. Mozafari, B. Alling, P. Steneteg, I.A. Abrikosov, Role of N defects in paramagnetic CrN at finite temperatures from first principles, *Phys. Rev. B* 91 (9) (2015), 094101.
 - [39] D. Depla, G. Buyle, J. Haemers, R. De Gryse, Discharge voltage measurements during magnetron sputtering, *Surf. Coat. Technol.* 200 (14–15) (2006) 4329–4338.
 - [40] D.M. Holzapfel, D. Music, S. Mráz, S.K. Aghda, M. Etter, P. Ondračka, M. Hans, D. Bogdanovski, S. Evertz, L. Patterer, Influence of ion irradiation-induced defects on phase formation and thermal stability of TiO₂. 27AlO₃. 52 coatings, *Acta Materialia* 237 (2022), 118160.
 - [41] C. Koller, N. Koutná, J. Ramm, S. Kolozsvári, J. Paulitsch, D. Holec, P. Mayrhofer, First principles studies on the impact of point defects on the phase stability of (Al_xCr_{1–x})₂O₃ solid solutions, *AIP Adv.* 6 (2) (2016), 025002.
 - [42] N. Koutná, D. Holec, O. Svoboda, F.F. Klimashin, P.H. Mayrhofer, Point defects stabilise cubic Mo–N and Ta–N, *J. Phys. D Appl. Phys.* 49 (37) (2016), 375303.
 - [43] K. Balasubramanian, S.V. Khare, D. Gall, Energetics of point defects in rocksalt structure transition metal nitrides: thermodynamic reasons for deviations from stoichiometry, *Acta Mater.* 159 (2018) 77–88.
 - [44] F.F. Klimashin, J. Kluson, M. Učík, M. Jilek, A. Lümekmann, J. Michler, T. Edwards, Nitrogen's whereabouts and role in structure-properties relationship of superstoichiometric Al–Cr–N, (in preparation).
 - [45] G. Håkansson, J.-E. Sundgren, D. McIntyre, J. Greene, W.-D. Münz, Microstructure and physical properties of polycrystalline metastable TiO₂. 5AlO₃. 5N alloys grown by dc magnetron sputter deposition, *Thin Solid Films* 153 (1–3) (1987) 55–65.
 - [46] J.E. Greene, S.A. Barnett, J.E. Sundgren, A. Rockett, Low-energy ion/surface interactions during film growth from the vapor phase, in: T. Itoh (Ed.), *Ion Beam Assisted Film Growth*, (1989), pp. 101–152.
 - [47] J. Kluson, M. Učík, M. Jilek, A. Lümekmann, High-power-density sputtering of industrial-scale targets: plasma analysis, (in preparation).
 - [48] I. Petrov, P.B. Barna, L. Hultman, J.E. Greene, Microstructural evolution during film growth, *Journal of Vacuum Science & Technology A* 21 (5) (2003) S117–S128.
 - [49] A. Anders, Tutorial: Reactive high power impulse magnetron sputtering (R-HiPIMS), *J. Appl. Phys.* 121 (17) (2017).
 - [50] W. Leroy, S. Mahieu, D. Depla, A. Ehasarian, High power impulse magnetron sputtering using a rotating cylindrical magnetron, *J. Vac. Sci. Technol. A* 28 (1) (2010) 108–111.
 - [51] W. Leroy, S. Konstantinidis, S. Mahieu, R. Snyder, D. Depla, Angular-resolved energy flux measurements of a dc-and HIPIMS-powered rotating cylindrical magnetron in reactive and non-reactive atmosphere, *J. Phys. D Appl. Phys.* 44 (11) (2011), 115201.
 - [52] L. Toth, *Transition Metal Carbides and Nitrides* (1971).
 - [53] L. Hultman, J. Sundgren, Structure/property relationships for hard coatings, in: R. Bunshah (Ed.), *Handbook of Hard Coatings: Deposition Technologies, Properties and Applications*, (2001), pp. 108–180.
 - [54] P.H. Mayrhofer, C. Mitterer, L. Hultman, H. Clemens, Microstructural design of hard coatings, *Prog. Mater. Sci.* 51 (8) (2006) 1032–1114.
 - [55] C.-S. Shin, D. Gall, N. Hellgren, J. Patscheider, I. Petrov, J. Greene, Vacancy hardening in single-crystal TiN x (001) layers, *J. Appl. Phys.* 93 (10) (2003) 6025–6028.
 - [56] S.K. Aghda, D. Music, Y. Unutulmazsoy, H.H. Sua, S. Mráz, M. Hans, D. Primetzhofer, A. Anders, J.M. Schneider, Unravelling the ion-energy-dependent structure evolution and its implications for the elastic properties of (V, Al) N thin films, *Acta Mater.* 214 (2021), 117003.
 - [57] J.E. Sundgren, Structure and Properties of Tin Coatings, *Thin Solid Films* 128 (1–2) (1985) 21–44.
 - [58] I. Petrov, L. Hultman, U. Helmersson, J.-E. Sundgren, J. Greene, Microstructure modification of TiN by ion bombardment during reactive sputter deposition, *Thin Solid Films* 169 (2) (1989) 299–314.
 - [59] Z. Zhang, A. Ghasemi, N. Koutná, Z. Xu, T. Grünstäudl, K. Song, D. Holec, Y. He, P.H. Mayrhofer, M. Bartosik, Correlating point defects with mechanical properties in nanocrystalline TiN thin films, *Mater. Des.* 207 (2021), 109844.
 - [60] H.S. Kim, M.B. Bush, The effects of grain size and porosity on the elastic modulus of nanocrystalline materials, *Nanostruct. Mater.* 11 (3) (1999) 361–367.
 - [61] F.F. Klimashin, L. Lobmaier, N. Koutná, D. Holec, P.H. Mayrhofer, The MoN–TaN system: role of vacancies in phase stability and mechanical properties, *Mater. Des.* 202 (2021), 109568.
 - [62] S. Ulrich, H. Holleck, J. Ye, H. Leiste, R. Loos, M. Stüber, P. Pesch, S. Sattel, Influence of low energy ion implantation on mechanical properties of magnetron sputtered metastable (Cr, Al) N thin films, *Thin Solid Films* 437 (1–2) (2003) 164–169.
 - [63] D.T. Quinto, Mechanical property and structure relationships in hard coatings for cutting tools, *J. Vac. Sci. Technol. A* 6 (3) (1988) 2149–2157.
 - [64] Z.-H. Xu, X. Li, Influence of equi-biaxial residual stress on unloading behaviour of nanoindentation, *Acta Mater.* 53 (7) (2005) 1913–1919.
 - [65] L. Karlsson, A. Hörling, M. Johansson, L. Hultman, G. Ramanath, The influence of thermal annealing on residual stresses and mechanical properties of arc-evaporated TiC_xN_{1–x} (x = 0, 0.15 and 0.45) thin films, *Acta Mater.* 50 (20) (2002) 5103–5114.
 - [66] N. Huber, J. Heerens, On the effect of a general residual stress state on indentation and hardness testing, *Acta Mater.* 56 (20) (2008) 6205–6213.
 - [67] M. Hans, L. Patterer, D. Music, D.M. Holzapfel, S. Evertz, V. Schnabel, B. Stelzer, D. Primetzhofer, B. Völker, B. Widrig, A.O. Eriksson, J. Ramm, M. Arndt, H. Rudigier, J.M. Schneider, Stress-dependent elasticity of TiAlN coatings, *Coatings* 9 (1) (2019) 24.
 - [68] R. Hoffman, The mechanical properties of thin condensed films, in: G. Hass, R. Thun (Eds.), *Physics of Thin Films*, (1966).
 - [69] M.F. Doerner, W.D. Nix, Stresses and Deformation Processes in Thin-Films on Substrates, *Crc Critical Reviews in Solid State and Materials Sciences* 14 (3) (1988) 225–268.
 - [70] H. Oettel, R. Wiedemann, S. Preissler, Residual stresses in nitride hard coatings prepared by magnetron sputtering and arc evaporation, *Surf. Coat. Technol.* 74 (1995) 273–278.
 - [71] G.C.A.M. Janssen, Stress and strain in polycrystalline thin films, *Thin Solid Films* 515 (17) (2007) 6654–6664.
 - [72] R. Daniel, K.J. Martinschitz, J. Keckes, C. Mitterer, The origin of stresses in magnetron-sputtered thin films with zone T structures, *Acta Mater.* 58 (7) (2010) 2621–2633.
 - [73] E. Chason, P.R. Guduru, Tutorial: Understanding residual stress in polycrystalline thin films through real-time measurements and physical models, *J. Appl. Phys.* 119 (19) (2016), 191101.
 - [74] G. Abadias, E. Chason, J. Keckes, M. Sebastiani, G.B. Thompson, E. Barthel, G. L. Doll, C.E. Murray, C.H. Stoessel, L. Martinu, Review article: stress in thin films and coatings: current status, challenges, and prospects, *J. Vac. Sci. Technol. A* 36 (2) (2018), 020801.

- [75] M. Bartosik, D. Holec, D. Apel, M. Klaus, C. Genzel, J. Keckes, M. Arndt, P. Polcik, C. Koller, P. Mayrhofer, Thermal expansion of Ti-Al-N and Cr-Al-N coatings, *Scr. Mater.* 127 (2017) 182–185.
- [76] D. Music, L. Banko, H. Ruess, M. Engels, A. Hecimovic, D. Grochla, D. Rogalla, T. Brögelmann, A. Ludwig, A. von Keudell, K. Bobzin, J.M. Schneider, Correlative plasma-surface model for metastable Cr-Al-N: Frenkel pair formation and influence of the stress state on the elastic properties, *J. Appl. Phys.* 121 (21) (2017), 215108.
- [77] J.-E. Sundgren, B.-O. Johansson, S.-E. Karlsson, H. Hentzell, Mechanisms of reactive sputtering of titanium nitride and titanium carbide II: Morphology and structure, *Thin Solid Films* 105 (4) (1983) 367–384.
- [78] B. Lawn, R. Wilshaw, Indentation fracture - principles and applications, *J. Mater. Sci.* 10 (6) (1975) 1049–1081.
- [79] A.G. Evans, E.A. Charles, Fracture toughness determinations by indentation, *J. Am. Ceram. Soc.* 59 (7–8) (1976) 371–372.
- [80] R. Soler, S. Gleich, C. Kirchlechner, C. Scheu, J.M. Schneider, G. Dehm, Fracture toughness of Mo₂BC thin films: intrinsic toughness versus system toughening, *Mater. Des.* 154 (2018) 20–27.
- [81] S. Massl, W. Thomma, J. Keckes, R. Pippin, Investigation of fracture properties of magnetron-sputtered TiN films by means of a FIB-based cantilever bending technique, *Acta Mater.* 57 (6) (2009) 1768–1776.
- [82] A.M. Korsunsky, M. Sebastiani, E. Bemporad, Residual stress evaluation at the micrometer scale: analysis of thin coatings by FIB milling and digital image correlation, *Surf. Coat. Technol.* 205 (7) (2010) 2393–2403.
- [83] G.T. Hahn, The influence of microstructure on brittle-fracture toughness, *Metall Trans A* 15 (6) (1984) 947–959.
- [84] S.M. Wiederhorn, Brittle-fracture and toughening mechanisms in ceramics, *Annu. Rev. Mater. Sci.* 14 (1) (1984) 373–403.
- [85] S. Liu, J.M. Wheeler, C. Davis, W. Clegg, X. Zeng, The effect of Si content on the fracture toughness of CrAlN/Si₃N₄ coatings, *J. Appl. Phys.* 119 (2) (2016), 025305.
- [86] A.G. Evans, Perspective on the development of high-toughness ceramics, *J. Am. Ceram. Soc.* 73 (2) (1990) 187–206.
- [87] R.O. Ritchie, The conflicts between strength and toughness, *Nat. Mater.* 10 (11) (2011) 817–822.
- [88] L. Liu, Q. Yu, Z. Wang, J. Ell, M.X. Huang, R.O. Ritchie, Making ultrastrong steel tough by grain-boundary delamination, *Science* 368 (6497) (2020) 1347–1352.
- [89] M. Gell, E. Smith, The propagation of cracks through grain boundaries in polycrystalline 3% silicon-iron, *Acta Metall.* 15 (2) (1967) 253–258.
- [90] T. Watanabe, S. Tsunekawa, Toughening of brittle materials by grain boundary engineering, *Mat Sci Eng a-Struct* 387 (2004) 447–455.
- [91] R. Daniel, M. Meindlhumer, W. Baumegeger, J. Zalesak, B. Sartory, M. Burghammer, C. Mitterer, J. Keckes, Grain boundary design of thin films: Using tilted brittle interfaces for multiple crack deflection toughening, *Acta Mater.* 122 (2017) 130–137.
- [92] R. Daniel, M. Meindlhumer, W. Baumegeger, J. Todt, J. Zalesak, T. Ziegelwanger, C. Mitterer, J. Keckes, Anisotropy of fracture toughness in nanostructured ceramics controlled by grain boundary design, *Mater. Des.* 161 (2019) 80–85.
- [93] M. Schlogl, C. Kirchlechner, J. Paulitsch, J. Keckes, P.H. Mayrhofer, Effects of structure and interfaces on fracture toughness of CrN/AlN multilayer coatings, *Scr. Mater.* 68 (12) (2013) 917–920.
- [94] R. Hahn, M. Bartosik, R. Soler, C. Kirchlechner, G. Dehm, P.H. Mayrhofer, Superlattice effect for enhanced fracture toughness of hard coatings, *Scr. Mater.* 124 (2016) 67–70.
- [95] R. Hahn, A.A. Tymoszyk, T. Wojcik, E. Ntemou, O. Hunold, P. Polcik, S. Kolozsvari, D. Primetzhof, P.H. Mayrhofer, H. Riedl, Unraveling the superlattice effect for hexagonal transition metal diboride coatings, *Scr. Mater.* 235 (2023).
- [96] R. Daniel, M. Meindlhumer, J. Zalesak, W. Baumegeger, J. Todt, T. Ziegelwanger, J.F. Keckes, C. Mitterer, J. Keckes, Multi-scale interface design of strong and damage resistant hierarchical nanostructured materials, *Mater. Des.* 196 (2020), 109169.
- [97] L. Porz, A.J. Klomp, X. Fang, N. Li, C. Yildirim, C. Detlefs, E. Bruder, M. Höfling, W. Rheinheimer, E.A. Patterson, Dislocation-toughened ceramics, *Mater. Horiz.* 8 (5) (2021) 1528–1537.
- [98] J.P. Best, J. Zechner, J.M. Wheeler, R. Schoepner, M. Morstein, J. Michler, Small-scale fracture toughness of ceramic thin films: the effects of specimen geometry, ion beam notching and high temperature on chromium nitride toughness evaluation, *Phil. Mag.* 96 (32–34) (2016) 3552–3569.
- [99] M. Bartosik, C. Rumeau, R. Hahn, Z.L. Zhang, P.H. Mayrhofer, Fracture toughness and structural evolution in the TiAlN system upon annealing, *Sci Rep-Uk* 7 (1) (2017) 16476.
- [100] A. Leyland, A. Matthews, On the significance of the H/E ratio in wear control: a nanocomposite coating approach to optimised tribological behaviour, *Wear* 246 (1–2) (2000) 1–11.
- [101] T. Tsui, G. Pharr, W. Oliver, C. Bhatia, R. White, S. Anders, A. Anders, I. Brown, Nanoindentation and nanoscratching of hard carbon coatings for magnetic disks, *MRS Proc.* (1995) 447.
- [102] X.Z. Ding, X.T. Zeng, Y.C. Liu, Structure and properties of CrAlSiN Nanocomposite coatings deposited by lateral rotating cathod arc, *Thin Solid Films* 519 (6) (2011) 1894–1900.
- [103] W.M. Seidl, M. Bartosik, S. Kolozsvari, H. Bolvardi, P.H. Mayrhofer, Influence of coating thickness and substrate on stresses and mechanical properties of (Ti, Al, Ta)N/(Al, Cr)N multilayers, *Surf. Coat. Technol.* 347 (2018) 92–98.
- [104] X. Chen, Y. Du, Y.-W. Chung, Commentary on using H/E and H₃/E₂ as proxies for fracture toughness of hard coatings, *Thin Solid Films* 688 (2019), 137265.
- [105] B.D. Beake, The influence of the H/E ratio on wear resistance of coating systems—Insights from small-scale testing, *Surf. Coat. Technol.* 442 (2022), 128272.
- [106] F. Svahn, Å. Kassman-Rudolph, E. Wallén, The influence of surface roughness on friction and wear of machine element coatings, *Wear* 254 (11) (2003) 1092–1098.
- [107] S.S. Kim, J.G. Han, S.Y. Lee, Deposition behaviours of CrN films on the edge area by cathodic arc plasma deposition process, *Thin Solid Films* 334 (1–2) (1998) 133–139.
- [108] M. Meindlhumer, N. Jäger, S. Spor, M. Rosenthal, J. Keckes, H. Hruby, C. Mitterer, R. Daniel, J. Keckes, J. Todt, Nanoscale residual stress and microstructure gradients across the cutting edge area of a TiN coating on WCCo, *Scr. Mater.* 182 (2020) 11–15.
- [109] A.M. Hofer-Robylyk, K.-H. Pichler, C. Linke, R. Franz, J. Winkler, C. Mitterer, Linking erosion and sputter performance of a rotatable Mo target to microstructure and properties of the deposited thin films, *Surf. Coat. Technol.* 352 (2018) 354–359.
- [110] D. Rafaja, C. Wustefeld, C. Baetz, V. Klemm, M. Dopita, M. Motylenko, C. Michotte, M. Kathrein, Effect of internal interfaces on hardness and thermal stability of nanocrystalline Ti_{0.5}Al_{0.5}N coatings, *Metallurgical and Materials Transactions a-Physical Metallurgy and Materials Science* 42 (a(3)) (2011) 559–569.
- [111] T. Chudoba, D. Schwenk, P. Reinstädt, M. Griepentrog, High-precision calibration of indenter area function and instrument compliance, *JOM* 74 (6) (2022) 2179–2194.
- [112] W.C. Oliver, G.M. Pharr, An improved technique for determining hardness and elastic-modulus using load and displacement sensing indentation experiments, *J. Mater. Res.* 7 (6) (1992) 1564–1583.
- [113] A.C. Fischer-Cripps, Critical review of analysis and interpretation of nanoindentation test data, *Surf. Coat. Technol.* 200 (14–15) (2006) 4153–4165.
- [114] F.F. Klimashin, P.H. Mayrhofer, Ab initio-guided development of super-hard Mo–Al–Cr–N coatings, *Scr. Mater.* 140 (2017) 27–30.
- [115] M. Sebastiani, K. Johanns, E.G. Herbert, F. Carassiti, G.M. Pharr, A novel pillar indentation splitting test for measuring fracture toughness of thin ceramic coatings, *Phil. Mag.* 95 (16–18) (2015) 1928–1944.
- [116] M. Ghidelli, M. Sebastiani, K.E. Johanns, G.M. Pharr, Effects of indenter angle on micro-scale fracture toughness measurement by pillar splitting, *J. Am. Ceram. Soc.* 100 (12) (2017) 5731–5738.